Check for updates

ADVANCED OPTICAL MATERIALS
www.advopticalmat.de

Multilayer Graphene/Epitaxial Silicon Near-Infrared Self-Quenched Avalanche Photodetectors

*Zongwen Li, Xiaoxue Cao, Zhixiang Zhang, Baoshi Qiao, Feng Tian, Yue Dai, Srikrishna Chanakya Bodepudi, Xinyu Liu, Jian Chai, Dajian Liu, Muhammad Abid Anwar, Xun Han, Fei Xue, Wenzhang Fang, Yaping Dan, Yuda Zhao, Huan Hu, Bin Yu, Chao Gao, and Yang Xu**

2D materials and their heterostructures exhibit considerable potential in the development of avalanche photodetectors (APDs) with high gain, response, and signal-to-noise ratio. These materials hold promise in addressing inherent technical challenges associated with APDs, such as low light absorption coefficient, elevated noise current, and substantial power consumption due to high bias resulting in only moderate current gain. In this work, a macro-assembled graphene nanofilm (nMAG)/epitaxial silicon (epi-Si) vertical heterostructure photodetector with a responsivity of 0.38 A W^{-1} and a response time of 1.4 µs is reported. The photodetectors use high-quality nMAG as the absorption layer and a lightly-doped epi-Si layer as the multiplication region under the avalanche mode to provide a high responsivity (2.51 mA W^{-1}) and detectivity (2.67 × 10^{9} Jones) at 1550 nm, which can achieve high-resolution imaging. In addition, the APD displays a weak noise level and an avalanche gain of *M* = 1123. It can work with relatively low avalanche turn-on voltages and achieve self-quenching by switching from illumination to dark during avalanche multiplication, with a real-time data transfer rate of 38 Mbps in near-infrared light communication data links. The proposed structure enables the fabrication of high-performance APDs in the infrared range using complementary-metal-oxide-semiconductor (CMOS)-compatible processes.

1. Introduction

The avalanche photodetector (APD), a current multiplication device with internal gain that enables high sensitivity, is featured by small size, wide operating conditions, excellent detection efficiency, and high gain. These features make it the mainstream choice for detecting weak light signals in various photoelectric imaging and optical communication systems.[1,2] The APD typically works at high reverse bias, usually in the tens to hundreds of volts range. This high reverse bias allows for the separation and acceleration of photogenerated electron–hole pairs, creating a strong electric field that results in impact ionization, yielding more carriers with large kinetic energy.[3] Several types of APDs based on silicon (Si), germanium (Ge), and III–V compound semiconductors have been recently reported.[4–7] Among these, APDs based on Ge and III–V semiconductor materials have been widely used for detection in the near-infrared (NIR) band due to their narrow bandgap feature.[8] However, the hole–electron dissociation ratio (*k*-value) of these APDs is close to 1, resulting in a large excess noise making it difficult to further enhance device performance.[9,10] Si semiconductor, possesses a very low *k*-value (<0.1), and exhibits low dark current and excellent multiplication properties, making it an ideal material to realize high carrier multiplication.[11] Due to the inherent bandgap of Si, its response band lies mainly in the visible region. To be specific, it is not suitable for optoelectronic

Z. Li, X. Cao, Z. Zhang, F. Tian, Y. Dai, S. C. Bodepudi, X. Liu, J. Chai, D. Liu, M. A. Anwar, X. Han, F. Xue, W. Fang, Y. Zhao, B. Yu, Y. Xu
College of Integrated Circuits
ZJU-Hangzhou Global Scientific and Technological Innovation Center
State Key Laboratory of Silicon and Advanced Semiconductor Materials
Zhejiang University
Hangzhou 310027, China
E-mail: yangxu-isee@zju.edu.cn

The ORCID identification number(s) for the author(s) of this article can be found under https://doi.org/10.1002/adom.202400335

DOI: 10.1002/adom.202400335

X. Cao, C. Gao
MOE Key Laboratory of Macromolecular Synthesis and Functionalization
Department of Polymer Science and Engineering
Zhejiang University
Hangzhou 310027, China

B. Qiao, F. Tian, H. Hu, Y. Xu
ZJU-UIUC Joint Institute, International Campus
Zhejiang University
Haining 314400, China

Y. Dan
National Key Laboratory of Science and Technology on Micro/Nano Fabrication
Shanghai Jiao Tong University
Shanghai 200240, China

© 2024 Wiley-VCH GmbH

devices with 1550 nm wavelength, which is commonly used in optical communications.[8] Therefore, improved Si-based APDs enabling sensitive detection in the NIR spectrum are required, particularly in the communication band. To this end, the most suitable approach is to fabricate a heterojunction APD with the combination of a material with Si that can extend the operating bandwidth beyond the communication band.

In recent years, the rise of atomically thin 2D materials has attracted great research interest in the field of optoelectronic devices due to their outstanding optoelectronic properties.[12–14] However, practical applications based on their photodetectors have been limited due to the low light absorption coefficients of 2D materials.[15] Designing APD device schemes with 2D materials that can effectively exploit the impact ionization of photogenerated carriers is a promising way to achieve a high gain response. However, the 2D material acts as both an absorbing and multiplication region, which inevitably introduces large noise currents that can interfere with the accurate detection of weak light signals.[16,17] Furthermore, most 2D APDs reported to date rely on a large bias to induce impact ionization because of the large back-to-back Schottky barrier between the 2D semiconductor channel material and the metal contact.[18,19] Graphene is an attractive 2D material because it possesses unique features, such as thin thickness, fast carrier mobility, narrow bandgap, and toughness.[20] Single-layer graphene (SLG) makes a van der Waals contact with the semiconductor, which results in a junction that inhibits the dark currents and device noise. SLG has limited light absorption of 2.3%, affecting the performance of its photodetectors.[21] Macro-assembled graphene nanofilms (nMAG) are promising for high-performance photodetectors due to their large-area uniform synthesis, high crystallinity, and controllable thickness.[22] They absorb 40% of light in infrared and can adhere atomically to substrates.[23–25] To achieve high-performance APDs with low noise current, high responsivity, and large gain, a thick but high-quality nMAG for the light-absorption layer and Si with a low hole–electron dissociation ratio as a carrier multiplication layer are needed.

In this work, a spectrum-dependent photodetector with low-defect density heterojunction and excellent performance was fabricated by integrating nMAG with epitaxial-silicon (epi-Si). Notably, to take great advantage of the high absorption coefficient of nMAG and the low impact ionization coefficient ratio of epi-Si, the nMAG was transferred onto the epi-Si surface as a main light-absorption layer, and the lightly-doped epi-Si acted as the photogenerated electron multiplication region. The heavily doped substrate-silicon enables the formation of an Ohmic contact between the Si semiconductor and the metal electrode. The nMAG/epi-Si heterojunction photodetector with self-quenching and high gain under the avalanche mode could operate at a communication wavelength of 1550 nm. The results showed that the responsivity and detectivity can be increased by more than three orders of magnitude without multiplication. The photodetector has a low avalanche turn-on voltage and a low noise, making it a low-power device for NIR detection at room temperature. This work opens the way to the application of nMAG combined with epi-Si for high-performance NIR detection and also facilitates the integration between optical communication and electronics in the NIR spectrum.

2. Results and Discussion

2.1. Device Structure and Basic Properties

Figure S1 (Supporting Information) illustrates a four-step synthesis procedure for preparing wafer-level uniform nMAG using filtration and high-temperature calcination treatment.[22] The preparation details are presented in the Experimental Section. High crystalline nMAG (scanning electron microscope (SEM) morphological map in Figure S2a, Supporting Information) with a few wrinkles but a flat surface was transferred on lightly-doped epi-Si to form the nMAG/epi-Si heterojunction device, as shown schematically in **Figure 1a**. The transmission electron microscopy (TEM) topographic view (Figure S2b, Supporting Information) combined with the negligible D peak (1330 cm^{-1}) in the Raman spectrum (Figure S2d, Supporting Information) of nMAG and undetectable oxygen peak (531.5 eV) in the X-ray photoelectron spectroscopy (XPS) spectrum (Figure S2e, Supporting Information) prove the high-quality of nMAG. Atomic force microscope (AFM) and Raman spectrum are used to confirm that the nMAG has a bulk thickness of ≈45 nm (see Figure S2c,d, Supporting Information). The nMAG can be directly transferred on the substrate without polymer assistance, which enables the clean heterojunction with van der Waals contacts of nMAG and epi-Si at an atomic level (HR-TEM cross-sectional image: Figure 1b).

Additionally, to confirm that nMAG can effectively enable photoelectric conversion in the wide-spectrum range, the simulated absorption curves of the SLG/epi-Si and nMAG/epi-Si are compared and plotted in Figure S2f (Supporting Information). Absorption of nMAG/epi-Si is significantly higher than that of SLG/epi-Si, which means that nMAG provides a stronger photoelectric conversion efficiency. At the 1550 nm wavelength, an enormous resonance absorption enhancement phenomenon was observed.[26] Further, the light absorption characteristics of epi-Si and the nMAG/epi-Si structure are characterized via Fourier Transform Infrared (FTIR) (Figure 1c), which can reach 58%. The broadband infrared absorption contributes to the high responsivity at the communication wavelength.

The nMAG/epi-Si device has a low Schottky barrier height (SBH) of 0.31 eV, which confirms its ability to detect infrared light. This can be deduced from the I–V curves of the device in the dark at different temperatures (as shown in Figure 1d; Figure S3, Supporting Information). The rectification ratio, defined as the ratio of the forward to the reverse current at ±1 V, decreases with increasing temperature. This is due to the reverse current increasing at a faster rate than the forward current with temperature. Besides, the parameters of the device were also calculated by dark current (Figure S4, Supporting Information), from which we get the same value (SBH ≈0.31 eV, ideal factor (n) ≈2.15, and series resistance (R_s) ≈300 Ω). The good repeatability of nMAG/epi-Si device performance is also demonstrated in Figure S5 (Supporting Information). To assess the quality of the interface between the nMAG and epi-Si materials, the noise-spectral-density (NSD) was tested (Figure 1e; Figure S6, Supporting Information). The NSD (S_I) value of 10^{-26} A^2 Hz^{-1}, at a −1 V bias, indicates a relatively high signal-to-noise ratio (SNR) and a clean surface. This is an improvement compared to SLG/Si devices.[24]

 © 2024 Wiley-VCH GmbH

21951071, 2024, 21, Downloaded from https://onlinelibrary.wiley.com/doi/10.1002/adom.202400335 by Zhejiang University, Wiley Online Library on [28/07/2024]. See the Terms and Conditions (https://onlinelibrary.wiley.com/terms-and-conditions) on Wiley Online Library for rules of use; OA articles are governed by the applicable Creative Commons License

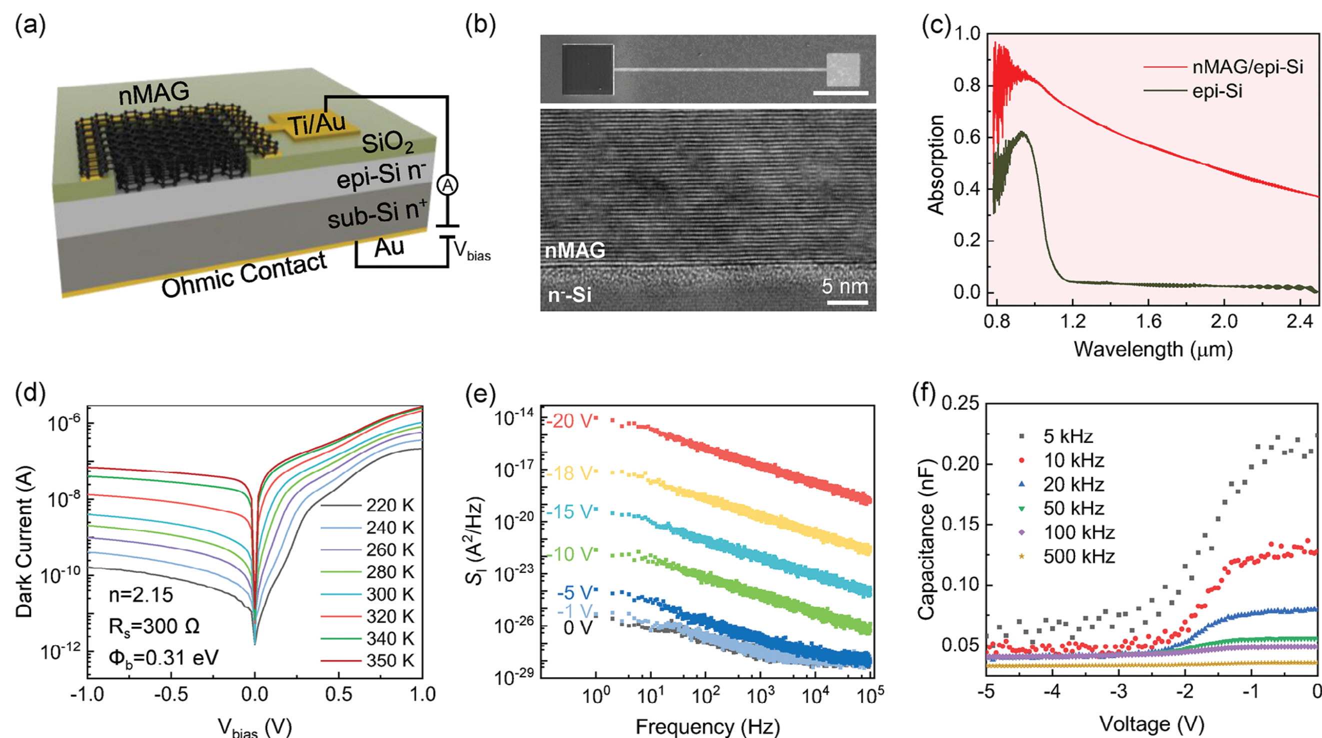

Figure 1. Schematic diagram and related characterization of the nMAG/epi-Si photodetector. Schematic illustration a), SEM image (scale bar is 500 μm), and cross-section HR-TEM image b) of the device. c) FTIR absorption spectra of nMAG/epi-Si structure and epi-Si wafer. d) *I*–*V* characteristics versus temperature ranging from 220 to 350 K. e) The NSD as a function of frequency at different biases. f) *C*–*V* curves measured at different frequencies.

Additionally, in avalanche devices, excess noise increases as the gain becomes higher due to the multiplication process. However, in our device, there is a weak noise level of only ≈10 pA at −10 V bias, as indicated in Figure S6 (Supporting Information). The carrier distribution and mobility of our device were further analyzed by capacitance–voltage (*C*–*V*) and admittance–voltage (*Y*–*V*) plots (Figure 1f; Figure S7, Supporting Information). The *C*–*V* curve presents a gradual decrease in capacitance as the applied reverse bias increases, which is mainly dominated by the barrier capacitance in the nMAG/epi-Si junction capacitance because most of the carriers are withdrawn from the space charge region (epi-Si depletion layer) making it extended.[27] This explanation is supported by the decreasing trend of admittance with increasing reverse bias in the *Y*–*V* plot (or impedance rising in the *Z*–*V* plot) shown in Figure S7 (Supporting Information). Additionally, the capacitance increases while the admittance decreases with decreasing frequency, which is attributed to the interface states on the epi-Si surface.[28]

2.2. Spectrum-Dependent Photoresponse under Illumination

Figures 2 and 3 show the evaluation of the photoresponse of the nMAG/epi-Si device at infrared wavelengths. Additionally, Figure 2a and Figure S8 (Supporting Information) demonstrate the results under illumination at the visible-NIR band, from 532 to 1064 nm. It is noted that the photocurrent increased as the power density increased under reverse bias, while the rectification ratio decreased. This is due to the significant alteration of the concentration of minority carriers by photogenerated carriers under reverse bias, which led to a photosensitive current. Furthermore, a remarkable photovoltaic behavior was displayed under light illumination at zero bias, suggesting the device can function without an external power supply. In order to evaluate the broadband and sensitive photoresponse behavior of our nMAG/epi-Si photodetector, we investigated the variation of four metrics, such as responsivity, external quantum efficiency (EQE), specific detectivity (D^*) and noise equivalent power (NEP), with the power density and the spectral response corresponding to the cutoff wavelength smaller than that of epi-Si. Figure 2b shows that the nMAG/epi-Si device exhibits a spectrum-dependent photoresponse in the 300–1100 nm range, with a responsivity peak of 0.38 A W^{-1}. The wavelength dependence of responsivity suggests that the generated photocurrent arises from epi-Si, as its shape closely follows the absorption spectrum of Si before the cutoff wavelength.[27] Additionally, the photodetector has an EQE of up to 60% in the visible region, but it decreases as the excitation wavelength increases in the NIR region. The D^* and NEP spectra of the nMAG/epi-Si photodetector over the 300–1100 nm wavelength range are presented in Figure 2c. The result shows that D^* and NEP can reach to 6.63×10^{12} Jones and 5.80×10^{-13} W Hz$^{-1/2}$, respectively.

The response speed, a critical parameter for evaluating photodetectors, is shown in Figure 2d. As the light source was rapidly switched ON/OFF, the device current responded with a correspondingly rapid change with excellent stability. The rise time (τ_r) and decay time (τ_d) of the device were measured at 1.4 and 1.6 μs, respectively, corresponding to the time for the device

 © 2024 Wiley-VCH GmbH

21951071, 2024, 21, Downloaded from https://onlinelibrary.wiley.com/doi/10.1002/adom.202400335 by Zhejiang University, Wiley Online Library on [28/07/2024]. See the Terms and Conditions (https://onlinelibrary.wiley.com/terms-and-conditions) on Wiley Online Library for rules of use; OA articles are governed by the applicable Creative Commons License

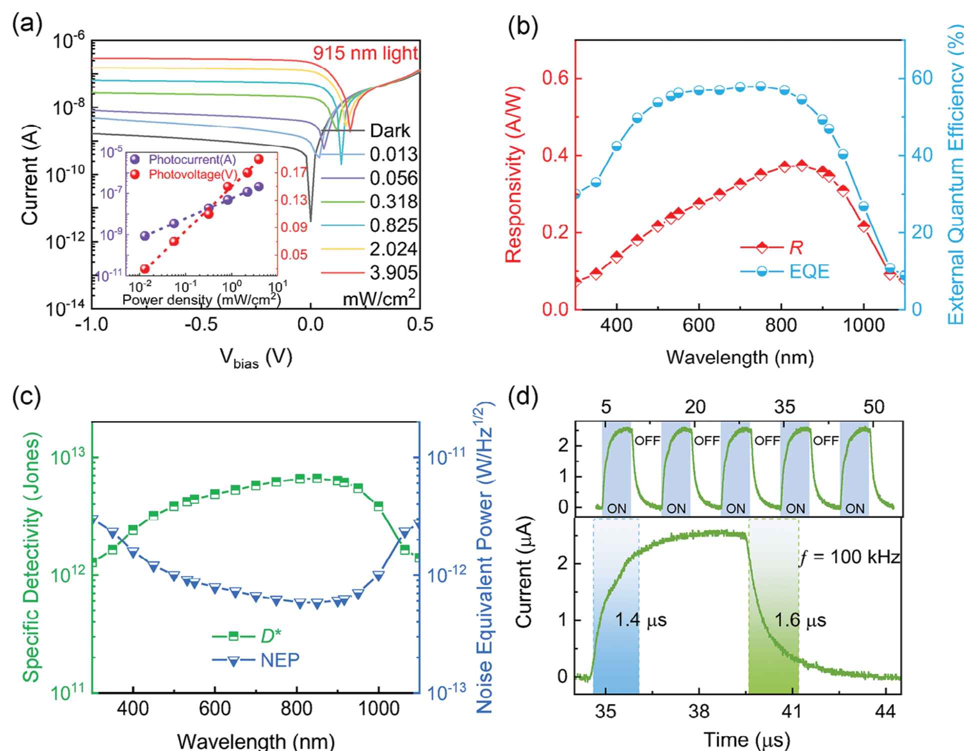

Figure 2. Spectrum-dependent and photoswitching behavior of nMAG/epi-Si photodetector. a) Logarithmic-scale *I–V* curves of the nMAG/epi-Si device as a function of 915 nm laser power densities. Spectral response for responsivity, external quantum efficiency b), specific detectivity, and noise equivalent power c) at −1 V bias. d) Time response of the nMAG/epi-Si device with a frequency of 100 kHz under the power density of 16.9 mW cm^{-2} at 915 nm.

current to increase (decrease) from 10% to 90% (from 90% to 10%) of the maximum value. With the *RC* time constant of ≈60 ns and the limitations of typical external circuits, the transient photo responses were measured to understand the intrinsic response speed of the device (see Figure S9a, Supporting Information). Figure S9b (Supporting Information) illustrates a τ_r of 66 ns and a τ_d of 434 ns under pulsed light irradiation. It is worth pointing out that the high stability and durability of our device is demonstrated by the time-resolved photoresponse (Figure S9c, Supporting Information) with reversible switching between high and low currents at different power densities.

2.3. Internal Photoelectron Emission Effect beyond Absorption Cutoff Wavelength

It should be mentioned here that the zero bandgap of nMAG and a low barrier height between nMAG and Si enable NIR communication and optical detection. The photoelectric conversion of nMAG was demonstrated via the photoconductive effect for detecting 915 and 1550 nm optical signals, as shown in Figure S10 (Supporting Information). Consequently, nMAG plays an important role in NIR detection, especially in the communication band. Figure 3a shows the *I–V* curves of the nMAG/epi-Si heterojunction photodetector under 1550 nm illumination. With the increasing power density, the photocurrent rises substantially, as shown in Figure 3b. The photocurrent and power density for Schottky junction photodiodes can be fitted using the equation $I = \alpha P^{\theta}$, in which the exponent θ characterizes the linearity of the device response against power density.[29] The value of θ is ≈0.94, indicating that the nMAG/epi-Si structure is close to an ideal Schottky junction with a low trap state density. As displayed in Figure 3c, the R and D^* values can reach 1.46 μA W^{-1} and 1.5 × 10^{6} Jones, respectively, under a weak power density of 1550 nm, where these parameters are independent of power density due to the limited excitation of carriers in nMAG from weak energy NIR photons.

To further understand the optoelectronic response of the nMAG/epi-Si heterojunction device, the energy band diagrams of the Schottky junction at reverse bias are presented in Figure S11 (Supporting Information). Due to the difference in work functions between the lightly doped epi-Si and nMAG, electrons tend to drift from epi-Si to nMAG. This phenomenon results in band bending at the lightly-doped epi-Si side because of the semi-metallic property of nMAG. At the same time, a strong built-in electric field is generated in the depletion region. Under low reverse bias, the expanded depletion region improves the separation efficiency of the photogenerated electron–hole pairs, thereby enabling more photocarriers to take part in photocurrent generation. In the case of nMAG/epi-Si heterojunction devices, the photoelectric conversion region can be divided into two types as shown in Figure 3d, due to the 1.12 eV bandgap of epi-Si. Photons with energies larger than the epi-Si bandgap can be absorbed by both epi-Si and nMAG, producing electron–hole pairs. However, the photon energy (0.5 hν > SBH) at λ > 1.1 μm is not sufficient to excite the carriers in Si, whereby the carriers in the nMAG are

© 2024 Wiley-VCH GmbH

21951071, 2024, 21, Downloaded from https://onlinelibrary.wiley.com/doi/10.1002/adom.202400335 by Zhejiang University, Wiley Online Library on [28/07/2024]. See the Terms and Conditions (https://onlinelibrary.wiley.com/terms-and-conditions) on Wiley Online Library for rules of use; OA articles are governed by the applicable Creative Commons License

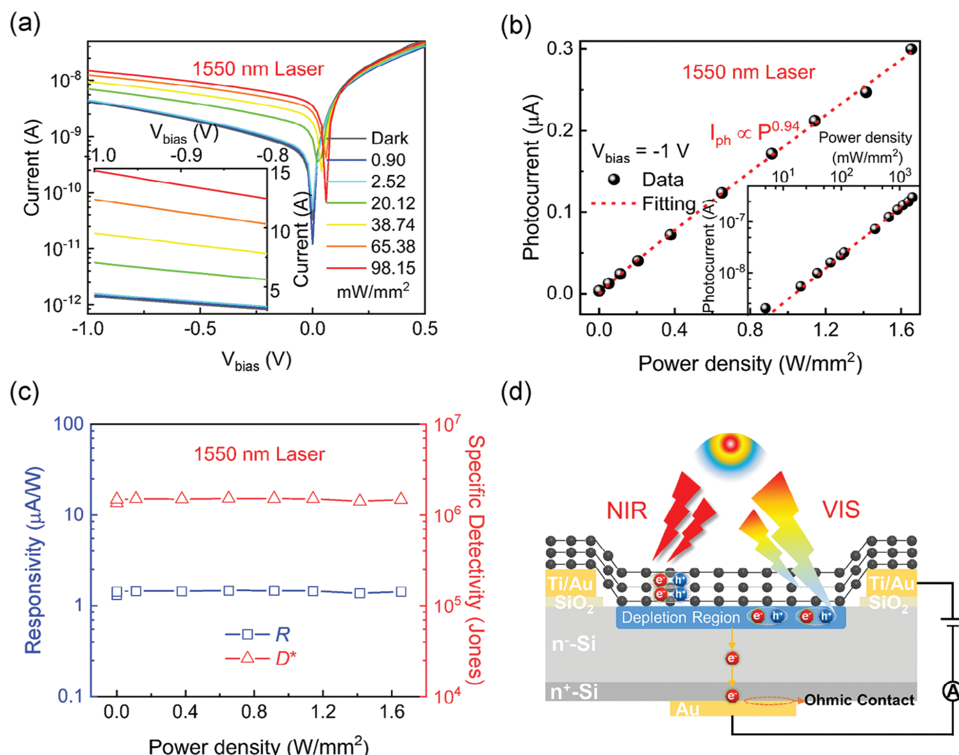

Figure 3. Characterization of the nMAG/epi-Si photodetector under 1550 nm irradiation. a) *I–V* curves of the device under various power densities. b) Photocurrent under different power densities at −1 V bias. The inset shows the photocurrent in the log scale. c) The responsivity and detectivity as a function of the power intensity. d) The mechanism for spectrum-dependent photoresponses of the nMAG/epi-Si photodetector under low reverse bias.

primarily excited by the internal photoelectron emission (IPE) effect, contributing to the photocurrent.[24,25]

2.4. Avalanche Multiplication Effect and Self-Quenching Feature under Bias

When the bias voltage is increased, the nMAG layer acts as the absorption layer for the NIR longwave spectrum in the nMAG/epi-Si device, as shown in **Figure** 4a. The lightly doped epi-Si layer, on the other hand, serves as the multiplication layer. By controlling the applied bias, the electric field in the nMAG layer can be adjusted, where light is absorbed and photocarriers are generated. The applied reverse bias separates photon-generated electron–hole pairs and drives electrons toward charge multiplication regions in epi-Si. Photogenerated electrons gain large kinetic energy under a large internal electric field in a relatively wide depletion region and avalanche multiplication can be achieved by impact ionization with valence electrons in the lattice, resulting in free electrons that grow exponentially causing the rapidly increasing photocurrent.

To further analyze this avalanche gain mechanism, we also investigated the effect of temperature on electrical breakdown in darkness. Here, the carrier generation mechanism mainly consists of the carrier thermal excitation effect and the internal multiplication effect in Si. The dark current decreases as temperature increases at any given voltage at which the more temperature-dependent internal multiplication effect dominates (Figure S12a, Supporting Information).[7,30] The clear increase in dark current with increasing temperature prior to electrical breakdown because the drift current increases in Si caused by external voltages. The threshold voltage exhibits a linear increase from −7.6 to −10.1 V as the temperature rises from 280 to 350 K. This trend is accompanied by a positive temperature coefficient of 0.03 V K^{-1}, as depicted in Figure S12b (Supporting Information). It is worth noting that the Zener tunneling effect typically results in a negative temperature coefficient, whereas a positive temperature-dependent trend is associated with the avalanche multiplication effect.[7,31,32] Phonon concentration increases with rising temperature in epi-Si and results in a quick loss in energy via electron–phonon collisions. Hence, only under stronger electric fields, carriers can obtain the energy required for impact ionization and avalanche multiplication. In Figure 4b, the *I–V* curves demonstrate that the current increases rapidly once the voltage surpasses a certain threshold. The breakdown voltage (V_{br}) gradually decreases from −13.5 to −11.9 V as the power density ranges from 0.11 to 1.14 W mm^{-2} (see inset of Figure 4b), which is much lower than the dark current (−23.7 V). The shift in threshold voltage supports the avalanche multiplication effect since the high-power density leads to an increase in the nMAG-excited photogenerated carriers, which promotes early impact ionization of electrons. Moreover, the high power density causes an uneven distribution of resistance, leading to a stronger electric field on nMAG and a greater impact ionization gain.[3]

To protect APDs from damage caused by large current density, the self-quenching behavior of the device is of great merit. Due

 © 2024 Wiley-VCH GmbH

21951071, 2024, 21, Downloaded from https://onlinelibrary.wiley.com/doi/10.1002/adom.202400335 by Zhejiang University, Wiley Online Library on [28/07/2024]. See the Terms and Conditions (https://onlinelibrary.wiley.com/terms-and-conditions) on Wiley Online Library for rules of use; OA articles are governed by the applicable Creative Commons License

21951071, 2024, 21, Downloaded from https://onlinelibrary.wiley.com/doi/10.1002/adom.202400335 by Zhejiang University, Wiley Online Library on [28/07/2024]. See the Terms and Conditions (https://onlinelibrary.wiley.com/terms-and-conditions) on Wiley Online Library for rules of use; OA articles are governed by the applicable Creative Commons License

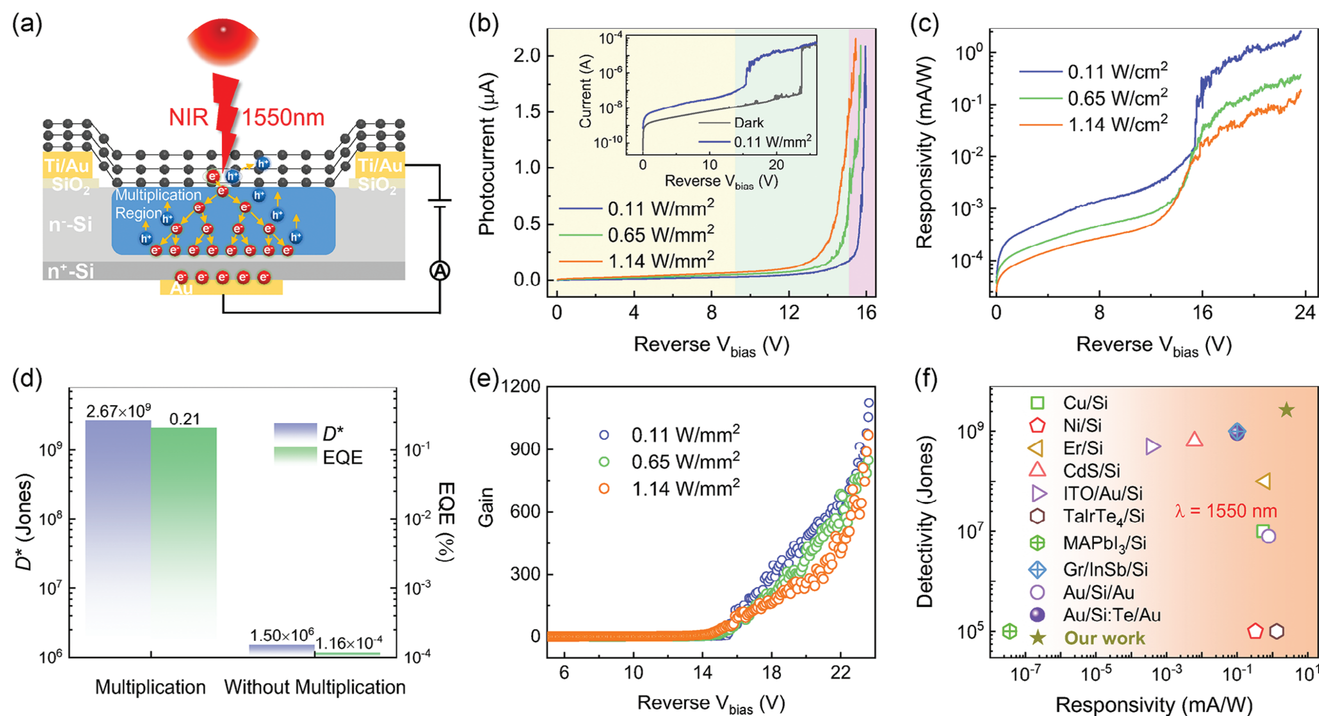

Figure 4. Working mechanism and avalanche multiplication characteristics of the nMAG/epi-Si APD. a) Mechanism of avalanche multiplication phenomena under large reverse bias. The reverse bias can accelerate the photo-generated electron toward the multiplication region (n^--Si). b) Dark current and photocurrent measurements at avalanche mode. Responsivity c) and Gain e) at different light power densities as the reverse voltage increases. d) Comparison of D^* and EQE of nMAG/epi-Si devices with and without avalanche multiplication. f) Photoresponsivity and detectivity at 1550 nm of our photodetector and previously reported heterojunction devices based on Si. Note that all device performance parameters (i.e., responsivity, detectivity, etc.) were characterized by using a uniform standard method.

to the illumination-dependent V_{br} mentioned above, avalanche self-quenching can be achieved for the nMAG/epi-Si photodetector. Based on the findings presented in Figure 4b, it was confirmed that the avalanche voltage of the device is higher when it is not illuminated compared to illuminated. If the operation voltage is set to −13.5 V, the avalanche breakdown will be initiated under 0.11 W mm^{-2} illumination at 1550 nm. On the other hand, in the absence of illumination, the avalanche voltage of the device increases to −23.7 V. When the device is not illuminated and the breakdown voltage is higher than the present operating voltage, the avalanche breakdown inside the device will automatically quench, and as a result, the current will drop quickly. The self-quenching mechanism observed in the nMAG/epi-Si photodetector safeguards against operational malfunctions, thereby extending its lifespan. The avalanche multiplication process in this device is triggered exclusively by incident light, but only if the operating voltage is optimized to a critical level.

These results demonstrate that avalanche multiplication dominates the internal gain. The gain of 1123 (Figure 4e) is yielded using the equation $M = I_{ph}/I_{ph0}$ at a relatively small reverse bias, where I_{ph} and I_{ph0} are the photocurrents with and without multiplication, respectively. The responsivity value of 2.51 mA W^{-1} is obtained, which is three orders of magnitude higher than that of the photodiode without multiplication (Figure 4c). The responsivity decreases with increasing power density after the multiplication effect, demonstrating the excellent detection ability of this device for weak light signals. The D^* and EQE of the device under avalanche can reach 2.67×10^9 Jones and 0.21% under 1550 nm light illumination, which is higher than the photodiode without avalanche (indicated in Figure 4d). The heterostructure photodetectors based on Si and other materials are presented as shown in Figure 4f and Table S1 (Supporting Information).[33–43] Because of the avalanche effect, the nMAG/epi-Si photodetector exhibits excellent performance when compared with the previous research results, including a low dark current, high responsivity, and detectivity, as well as a fast response time.

2.5. Communication and Imaging System at NIR

The nMAG/epi-Si photodetector was integrated into an optical communication system as an optical signal receiver to measure the eye diagram, further demonstrating its feasibility in practical optical applications. **Figure 5a** presents the schematic diagram of a visible light communication system. The optical signal for testing the eye diagram was generated by an arbitrary waveform generator (AWG) that outputs a random signal. The signal is then amplified by an electrical amplifier to drive the NIR laser. The eight groups of serial signal numbers are shown in Figure S13 (Supporting Information), where the afterglow of the oscilloscope overlaps each of the resulting code element waveforms from the scan to create an eye diagram (see Figure 5b). The collected eye diagram is relatively clear and open up to at least 38 Mbps, indicating the accuracy of the high-speed data transfer.

© 2024 Wiley-VCH GmbH

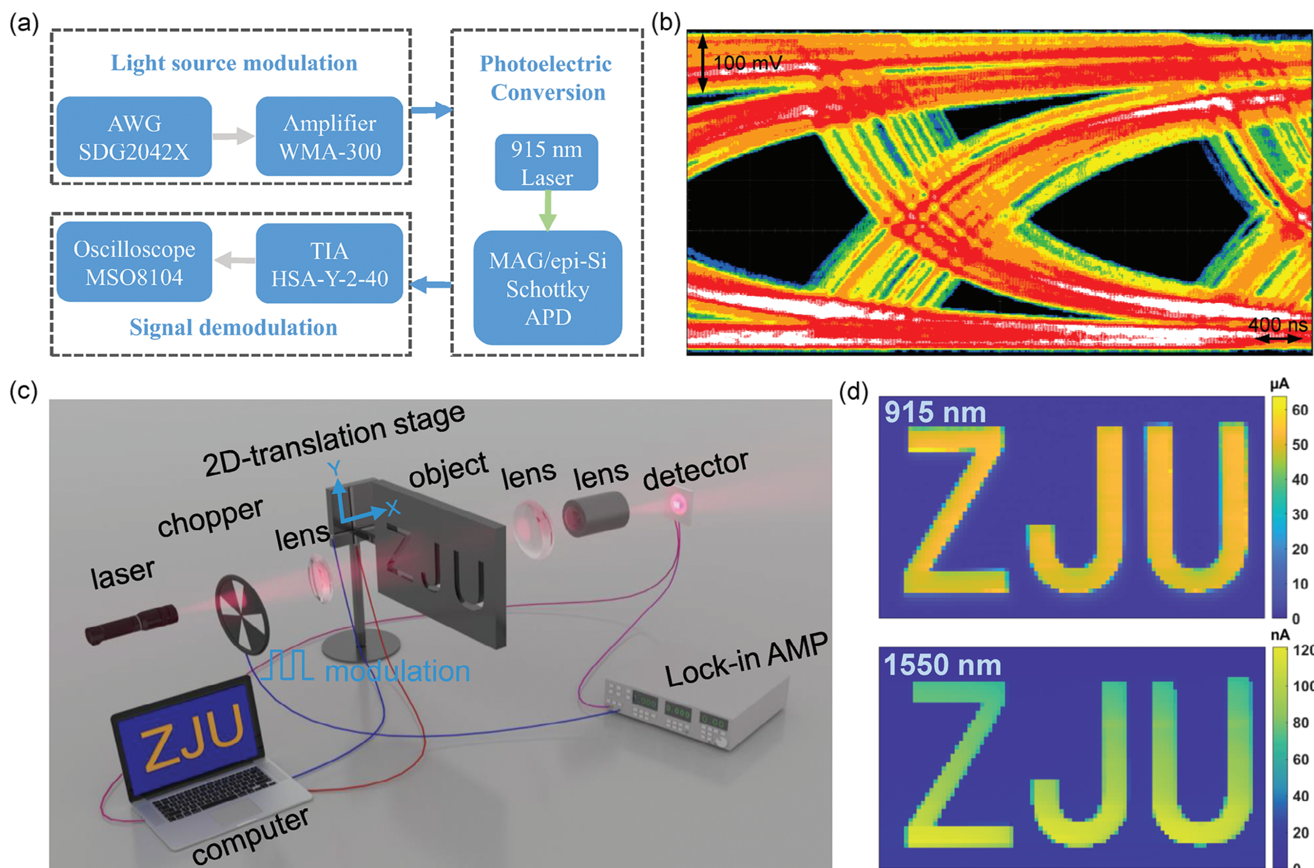

Figure 5. Performance characterization of NIR light communication. a) NIR light communication test diagram using our photodetector as a light signal receiver. b) A clear eye diagram corresponding to 38 Mbps data rates. c) Diagram illustration of the image sensor systems. d) Dual-color (Top: shortwave NIR, power density: 456.15 mW cm^{-2}@915 nm; Bottom: longwave NIR, power density: 8.25 W mm^{-2}@1550 nm) image of the "ZJU" logo obtained from our nMAG/epi-Si photodetector system.

Furthermore, the nMAG/epi-Si photodetector was used to investigate the imaging capability. Combined with external readout circuitry, the nMAG/epi-Si photodetector was packed into an imaging system using scanning acquisition of image data (Figure 5c). The imaging object, a mask of the hollow abbreviated letters "ZJU", can be moved continuously in horizontal and vertical directions through a computerized 2D-translation stage. The NIR images with 52 × 92 pixels were available with external power, via converting the output signal current from the photodetector captured by the computer into "gray code". Figure 5d presents the dual-color images for the object "ZJU" with sharp boundaries captured by the nMAG/epi-Si photodetector under NIR irradiation at room temperature. The transfer of wafer-level freestanding nMAGs and integration with epi-Si offers the opportunity to develop CMOS-compatible room temperature NIR image sensors.

3. Conclusion

In conclusion, a photodetector based on a heterojunction structure composed of nMAG and epi-Si is fabricated, which presents a 0.38 A W^{-1} responsivity and a 1.4 µs response time at NIR. Internal multiplication is observed at a relatively small reverse bias, with extracted gain value reaching up to $M = 1123$, which is higher than most reported APDs based on 2D materials. The device shows a high responsivity of 2.51 mA W^{-1} and a detectivity of 2.67 × 10^{9} Jones at 1550 nm in the avalanche multiplication. Moreover, this photodetector also exhibits a low noise current of ≈10 pA. The observed fast response of the device allows a maximum real-time data transfer rate of 38 Mbps when used in NIR communication data links. Furthermore, the photodetector can be used for dual-color detection and was successfully used to record images. This work provides guidance for the development of optical communication devices and NIR image sensors based on 2D/Si heterostructures.

4. Experimental Section

Preparation of nMAG: The primary material for preparing wafer-level nMAG was defective graphene oxide (GO), which was supplied by Hangzhou Gaoxi Technology Co., Ltd. The GO sheet dispersion was first diluted and sonicated for uniform distribution before being filtered under vacuum conditions using a 24 mm radius AAO filter (Whatman, pore size 0.2 mm) to produce a supported GO membrane on the AAO filter (i.e., GO/AAO film). A camphor/reduced graphene oxide (rGO)/AAO film was obtained by reducing the GO to rGO with HI vapor at 60 °C and depositing

 © 2024 Wiley-VCH GmbH

21951071, 2024, 21, Downloaded from https://onlinelibrary.wiley.com/doi/10.1002/adom.202400335 by Zhejiang University, Wiley Online Library on [28/07/2024]. See the Terms and Conditions (https://onlinelibrary.wiley.com/terms-and-conditions) on Wiley Online Library for rules of use; OA articles are governed by the applicable Creative Commons License

camphor on the surface of the rGO film at 120 °C. The camphor/rGO/AAO film was cooled to room temperature and the camphor/rGO membrane was automatically separated from the AAO membrane due to the shrinkage effect of the camphor membrane during rapid cooling. The camphor was removed to leave a separate rGO film using a continuous temperature of 60 °C. Lastly, the separate rGO film was further heated in an Ar-protected high-temperature graphite furnace (NTG-SML-50L) at 2800 °C to produce nMAG with healing defects. The thickness of nMAG depends on the mass loading of the GO sheet dispersion.

Device Fabrication: An n-type lightly-doped (10^{15} cm^{-3}) epi-Si on the n-type heavily-doped (10^{19} cm^{-3}) Si substrate wafer was used and cleaned by the standard cleaning process. The thicknesses of lightly doped epi-Si and heavily doped Si substrates were 8.5 and 625 µm, respectively. A 100 nm thickness SiO_2 was grown by thermal oxidation as an insulating layer. A Ti/Au (10 nm/50 nm) top electrode was deposited onto the front side of a SiO_2/Si substrate via UV lithography (MA6-BSA) and magnetron sputtering (DISCOVERY-635) processes. Next, the SiO_2 dielectric layer in specific areas was etched away through lithography patterning and buffered oxide etchant (BOE) to form a Si window (500 × 500 µm). A mixture of ethanol and pure water was then dropped onto the processed Si substrate surface, followed by transferring a 45 nm-nMAG and blowing it with N_2 to make close contact. Excess nMAG beyond the device electrode was etched via further lithography and an Inductively Coupled Plasma Dry Etching System (OXFORD, Plasmapro100 Cobra 180). The bottom electrode was directly contacted with the heavily doped area in the epi-Si wafer to complete Ohmic contact. Finally, the defective state of the nMAG/epi-Si interface was reduced by high-temperature (400 °C) annealing in an inert gas atmosphere (N_2) using a rapid annealing furnace (RTP-VT100M).

Characterization and Measurement: The Raman spectra of nMAG were measured via Raman spectroscopy (Renishaw inVia-Reflex) using a 532 nm excitation wavelength laser. Field emission SEM (Sigma300), AFM (WET-SPM-9500J3), XPS (PHI 5000C ESCA), and TEM (Hitachi H-9500) were used to identify its properties such as morphology, thickness, crystallinity, and flatness. Broad-spectrum absorption characterization of nMAG/epi-Si structure was also performed via FTIR Spectrometer (Nicolet iN10, Thermofisher Scientific). The NSD (S_I) were recorded by a noise measurement system (PDA NC300L, 100 kHz bandwidth). The capacitance and admittance were captured using a Keysight B1500 semiconductor device analyzer and a precision LCR meter (TH2828, Tonghui Electronics), respectively. Opto–electrical properties were measured with a Keithley 4200 semiconductor parameter analyzer under ambient/or vacuum conditions at different temperatures. The spectral response characteristics were measured from a response measurement system equipped with a monochromator (Zolix Instruments, China), a lock-in amplifier (Model OE1022, Guangzhou Sine Scientific Instrument Co. LTD), and a 150-W xenon lamp. The temporal response was observed with a digital oscilloscope (MSO8104, RIGOL Technologies Co. LTD.) and a trans-impedance amplifier (TIA, Model HSA-Y-2-40, Germany).

Supporting Information

Supporting Information is available from the Wiley Online Library or from the author.

Acknowledgements

This work was supported by the National Natural Science Foundation of China (Grant Nos. 92164106 and U22A2076), National Key Research and Development Program of China (Grant Nos. 2022YFA1204300, 2022YFA1204304, 2022YFA1204900), Fundamental Research Funds for the Central Universities (Grant Nos. 2021FZZX001-17), and Zhejiang University (ZJU) Micro-Nano Fabrication Center.

Conflict of Interest

The authors declare no conflict of interest.

Data Availability Statement

The data that support the findings of this study are available in the supplementary material of this article.

Keywords

avalanche photodetectors, epitaxial silicon, high avalanche gain, infrared detection, macro-assembled graphene nanofilms

Received: February 29, 2024
Revised: April 17, 2024
Published online: May 16, 2024

[1] S. Assefa, F. Xia, Y. A. Vlasov, *Nature*. **2010**, *464*, 80.
[2] S. Yanikgonul, V. Leong, J. R. Ong, T. Hu, S. Y. Siew, C. E. Png, L. Krivitsky, *Nat. Commun*. **2021**, *12*, 1834.
[3] Q. Zhang, N. Li, T. Zhang, D. Dong, Y. Yang, Y. Wang, Z. Dong, J. Shen, T. Zhou, Y. Liang, W. Tang, Z. Wu, Y. Zhang, J. Hao, *Nat. Commun*. **2023**, *14*, 418.
[4] X. Zeng, Z. Huang, B. Wang, D. Liang, M. Fiorentino, R. G. Beausoleil, *Optica*. **2019**, *6*, 772.
[5] A. H. Jones, S. D. March, S. R. Bank, J. C. Campbell, *Nat. Photonics*. **2020**, *14*, 559.
[6] J. Chen, J. Chen, X. Li, J. He, L. Yang, J. Wang, F. Yu, Z. Zhao, C. Shen, H. Guo, G. Li, X. Chen, W. Lu, *Npj Quantum Mater*. **2021**, *6*, 103.
[7] D. Chen, S. D. March, A. H. Jones, Y. Shen, A. A. Dadey, K. Sun, J. A. McArthur, A. M. Skipper, X. Xue, B. Guo, J. Bai, S. R. Bank, J. C. Campbell, *Nat. Photonics*. **2023**, *17*, 594.
[8] J. Miao, C. Wang, *Nano Res*. **2021**, *14*, 1878.
[9] P. Vines, K. Kuzmenko, J. Kirdoda, D. C. S. Dumas, M. M. Mirza, R. W. Millar, D. J. Paul, G. S. Buller, *Nat. Commun*. **2019**, *10*, 1086.
[10] Y. Ma, Y. Zhang, Y. Gu, X. Chen, Y. Shi, W. Ji, S. Xi, B. Du, X. Li, H. Tang, Y. Li, J. Fang, *Opt. Express*. **2016**, *24*, 7823.
[11] R. H. Hadfield, *Nat. Photonics*. **2009**, *3*, 696.
[12] J. An, X. Zhao, Y. Zhang, M. Liu, J. Yuan, X. Sun, Z. Zhang, B. Wang, S. Li, D. Li, *Adv. Funct. Mater*. **2022**, *32*, 2110119.
[13] Y. Meng, J. Feng, S. Han, Z. Xu, W. Mao, T. Zhang, J. S. Kim, I. Roh, Y. Zhao, D.-H. Kim, Y. Yang, J.-W. Lee, L. Yang, C.-W. Qiu, S.-H. Bae, *Nat. Rev. Mater*. **2023**, *8*, 498.
[14] W. Liu, J. Lv, L. Peng, H. Guo, C. Liu, Y. Liu, W. Li, L. Li, L. Liu, P. Wang, S. C. Bodepudi, K. Shehzad, G. Hu, K. Liu, Z. Sun, T. Hasan, Y. Xu, X. Wang, C. Gao, B. Yu, X. Duan, *Nat. Electron*. **2022**, *5*, 281.
[15] Q. Qiu, Z. Huang, *Adv. Mater*. **2021**, *33*, 2008126.
[16] J. Seo, J. H. Lee, J. Pak, K. Cho, J. K. Kim, J. Kim, J. Jang, H. Ahn, S. C. Lim, S. Chung, K. Kang, T. Lee, *Adv. Sci*. **2021**, *8*, 2102437.
[17] J. Kim, K. Cho, J. Pak, W. Lee, J. Seo, J.-K. Kim, J. Shin, J. Jang, K.-Y. Baek, J. Lee, S. Chung, K. Kang, T. Lee, *ACS Nano*. **2022**, *16*, 5376.
[18] J. Pak, Y. Jang, J. Byun, K. Cho, T.-Y. Kim, J.-K. Kim, B. Y. Choi, J. Shin, Y. Hong, S. Chung, T. Lee, *ACS Nano*. **2018**, *12*, 7109.
[19] Y. Yang, J. Jeon, J.-H. Park, M. S. Jeong, B. H. Lee, E. Hwang, S. Lee, *ACS Nano*. **2019**, *13*, 8804.
[20] F. Bonaccorso, Z. Sun, T. Hasan, A. C. Ferrari, *Nat. Photonics*. **2010**, *4*, 611.
[21] C. Xie, Y. Wang, Z.-X. Zhang, D. Wang, L.-B. Luo, *Nano Today*. **2018**, *19*, 41.
[22] L. Peng, Y. Han, M. Wang, X. Cao, J. Gao, Y. Liu, X. Chen, B. Wang, B. Wang, C. Zhu, X. Wang, K. Cao, M. Huang, B. V. Cunning, J. Pang, W. Xu, Y. Ying, Z. Xu, W. Fang, Y. Lu, R. S. Ruoff, C. Gao, *Adv. Mater*. **2021**, *33*, 2104195.

 © 2024 Wiley-VCH GmbH

21951071, 2024, 21, Downloaded from https://onlinelibrary.wiley.com/doi/10.1002/adom.202400335 by Zhejiang University, Wiley Online Library on [28/07/2024]. See the Terms and Conditions (https://onlinelibrary.wiley.com/terms-and-conditions) on Wiley Online Library for rules of use; OA articles are governed by the applicable Creative Commons License

[23] L. Liu, X. Cao, L. Peng, S. C. Bodepudi, S. Wu, W. Fang, J. Liu, Y. Xiao, X. Wang, Z. Di, R. Cheng, Y. Xu, C. Gao, B. Yu, presented at *IEEE Int. Electron Devices Meeting (IEDM)*, San Francisco, CA, USA December **2021**.
[24] a) L. Peng, L. Liu, S. Du, S. C. Bodepudi, L. Li, W. Liu, R. Lai, X. Cao, W. Fang, Y. Liu, X. Liu, J. Lv, M. Abid, J. Liu, S. Jin, K. Wu, M.-L. Lin, X. Cong, P.-H. Tan, H. Zhu, Q. Xiong, X. Wang, W. Hu, X. Duan, B. Yu, Z. Xu, Y. Xu, C. Gao, *InfoMat.* **2022**, *4*, e12309. b) L. Liu, X. Cao, X. Liu, Z. Zhang, X. Wang, Y. Xu, *IEEE Trans. Nanotechnol.* **2022**, *21*, 307.
[25] X. Cao, L. Peng, L. Liu, J. Lv, Z. Li, F. Tian, Y. Dong, X. Liu, Y. Shen, H. Sun, Y. Xu, W. Fang, C. Gao, *Carbon.* **2022**, *198*, 244.
[26] C. Lin, M. L. Povinelli, *Opt. Express.* **2011**, *19*, A1148.
[27] A. Pelella, A. Grillo, E. Faella, G. Luongo, M. B. Askari, A. Di Bartolomeo, *ACS Appl. Mater. Interfaces.* **2021**, *13*, 47895.
[28] A. Di Bartolomeo, G. Luongo, F. Giubileo, N. Funicello, G. Niu, T. Schroeder, M. Lisker, G. Lupina, *2D Mater.* **2017**, *4*, 025075.
[29] J. Mao, B. Zhang, Y. Shi, X. Wu, Y. He, D. Wu, J. Jie, C.-S. Lee, X. Zhang, *Adv. Funct. Mater.* **2022**, *32*, 2108174.
[30] L. Jia, F. Huang, W. Zheng, *Adv. Opt. Mater.* **2022**, *10*, 2202138.
[31] Y. Wang, H. Li, J. Cao, J. Shen, Q. Zhang, Y. Yang, Z. Dong, T. Zhou, Y. Zhang, W. Tang, Z. Wu, *ACS Nano.* **2021**, *15*, 16654.
[32] X. Zhao, D. Jiang, M. Zhao, Y. Duan, *Adv. Opt. Mater.* **2021**, *9*, 2002023.
[33] Y. Dai, X. Wang, W. Peng, C. Xu, C. Wu, K. Dong, R. Liu, Z. Wang, *Adv. Mater.* **2018**, *30*, 1705893.
[34] T.-Y. Lin, K.-T. Lin, C.-C. Lin, Y.-W. Lee, L.-T. Shiu, W.-Y. Chen, H.-L. Chen, *Mater. Horiz.* **2019**, *6*, 1156.
[35] T. Crisci, L. Moretti, M. Gioffre, M. Iodice, G. Coppola, M. Casalino, *J. Eur. Opt. Soc.-Rapid.* **2020**, *16*, 6.
[36] X. Li, Z. Deng, J. Li, Y. Li, L. Guo, Y. Jiang, Z. Ma, L. Wang, C. Du, Y. Wang, Q. Meng, H. Jia, W. Wang, W. Liu, H. Chen, *Photon. Res.* **2020**, *8*, 1662.
[37] J. W. John, V. Dhyani, S. Maity, S. Mukherjee, S. K. Ray, V. Kumar, S. Das, *Nanotechnology.* **2020**, *31*, 455208.
[38] X. Li, T. Sun, K. Zhou, X. Hong, X. Tang, D. Wei, W. Feng, J. Shen, D. Wei, *Nanotechnology.* **2020**, *31*, 315204.
[39] Y.-C. Huang, V. Parimi, W.-C. Chang, H.-J. Syu, Z.-C. Su, C.-F. Lin, *IEEE Photonics J.* **2021**, *13*, 1.
[40] Z. Yang, H. Wang, L. Guo, Q. Zhou, Y. Gu, F. Li, S. Qiao, C. Pan, S. Wang, *Small.* **2021**, *17*, 2101572.
[41] M. Wang, E. Garcia-Hemme, Y. Berencen, R. Hubner, Y. Xie, L. Rebohle, C. Xu, H. Schneider, M. Helm, S. Zhou, *Adv. Opt. Mater.* **2021**, *9*, 2101798.
[42] L. Zhang, X. Han, P. Wen, S. Zhang, Z. Zheng, J. Li, W. Gao, *ACS Appl. Nano Mater.* **2022**, *5*, 6523.
[43] L. Zhang, W. Lu, R. Qian, H. Wang, H. Xu, L. Zhu, Z. An, *Appl. Phys. Lett.* **2023**, *122*, 031101.

© 2024 Wiley-VCH GmbH

21951071, 2024, 21, Downloaded from https://onlinelibrary.wiley.com/doi/10.1002/adom.202400335 by Zhejiang University, Wiley Online Library on [28/07/2024]. See the Terms and Conditions (https://onlinelibrary.wiley.com/terms-and-conditions) on Wiley Online Library for rules of use; OA articles are governed by the applicable Creative Commons License